JUNHO LEE[1], NAMHYUK SEO[1], SANG-HWA LEE[2], KWANGJUN EUH[2], SINGON KANG[3],
SEUNG BAE SON[1,4], SEOK-JAE LEE[1,4], JAE-GIL JUNG[1,4*]

EFFECT OF Al–5Ti–1B ADDITION ON SOLIDIFICATION MICROSTRUCTURE
AND HOT DEFORMATION BEHAVIOR OF DC-CAST Al–Zn–Mg–Cu ALLOY

This study investigated the effect of adding Al–5Ti–1B grain refiner on the solidification microstructure and hot deformation behavior of direct-chill (DC) cast Al–Zn–Mg–Cu alloys. The grain refiner significantly decreased the grain size and modified the morphology. Fine-grained (FG) alloys with grain refiners exhibit coarse secondary phases with a reduced number density compared to coarse-grained (CG) alloys without grain refiners. Dynamic recrystallization (DRX) was enhanced at higher compression temperatures and lower strain rates in the CG and FG alloys. Both particle stimulated nucleation (PSN) and continuous dynamic recrystallization (CDRX) are enhanced in the FG alloys, resulting in decreased peak stress values (indicating DRX onset) at 450°C. The peak stress of the FG alloys was higher at 300-400°C than that of the CG alloys because of grain refinement hardening over softening by enhanced DRX.

Keywords: Al–Zn–Mg–Cu alloy; Microstructure; Twinned dendrite; Hot deformation; Dynamic recrystallization

1. Introduction

Al–Zn–Mg–Cu (7xxx) wrought alloys are widely employed in automotive and aerospace industries owing to their excellent mechanical properties enhanced by precipitation strengthening [1]. Al–Zn–Mg–Cu wrought alloys are generally manufactured by casting, homogenization, hot deformation (e.g., hot extrusion and hot rolling), and solution and aging heat treatments [2-4]. It is important to understand and optimize the deformation process to manufacture high-quality Al–Zn–Mg–Cu alloy products with poor formability [5,6]. Many researchers have studied the hot deformation behavior of Al–Zn–Mg–Cu alloys, such as the evolution of texture and dynamic recrystallization (DRX) behavior [7,8] and the construction of processing maps for optimum deformation conditions [9-11].

Direct-chill (DC) casting is a commonly utilized process for wrought Al alloys owing to its low cost and high productivity [12]. At high dendrite growth rates, DC casting often results in twinned dendrite solidification via a lateral propagation mechanism [13]. The twinned dendrite inhibits the subsequent deformation process [14,15]. In Al–Zn–Mg–Cu alloys, grain refiner addition in DC casting modifies coarse columnar twinned

dendrites into fine equiaxed ones [16], thereby significantly affecting the hot deformation behavior. However, there are few reports on the effect of the solidification microstructure on the hot deformation behavior of DC-cast Al–Zn–Mg–Cu alloys.

Therefore, we investigated the effect of adding a grain refiner (Al–Ti–B master alloy) on the solidification microstructure of DC-cast Al–Zn–Mg–Cu alloys. The hot deformation behavior of DC-cast alloys at 300-450°C was examined by electron backscattered diffraction (EBSD) analysis, and the relationship between the solidification microstructure and recrystallization behavior was discussed.

2. Experimental

A commercial AA7068 (Al–7.7Zn–2.6Mg–2.1Cu–0.1Fe–0.01Ti, wt.%) ingot was used as the base material. AA7068 ingots with and without the Al–5Ti–1B master alloy (grain refiner) were melted and degassed using Ar gas bubbling filtration (GBF). A hot-top mold-type direct-chill (DC) caster was used for preparing AA7068 billets (50 mm diameter) with coarse-grain (CG) and fine-grain (FG) microstructures. The Ti contents of the CG

[1] JEONBUK NATIONAL UNIVERSITY, DIVISION OF ADVANCED MATERIALS ENGINEERING, JEONJU 54896, REPUBLIC OF KOREA
[2] KOREA INSTITUTE OF MATERIALS SCIENCE, ADVANCED METALS DIVISION, CHANGWON 51508, REPUBLIC OF KOREA
[3] DONG-A UNIVERSITY, DEPARTMENT OF MATERIALS SCIENCE AND ENGINEERING, BUSAN 49315, REPUBLIC OF KOREA
[4] JEONBUK NATIONAL UNIVERSITY, RESEARCH CENTER FOR ADVANCED MATERIALS DEVELOPMENT, JEONJU 54896, REPUBLIC OF KOREA

* Corresponding Author: jgjung@jbnu.ac.kr

and FG alloys were 0.01 and 0.04 wt.%, respectively. Details of the DC casting procedure can be found elsewhere [17].

Cylindrical specimens ($\Phi 8 \times 12$ mm) for the hot compression tests were machined from the central part of the billet to avoid surface chills. The cylindrical samples were homogenized at 450°C for 24 h and then hot-compressed at 300, 350, 400, and 450°C up to a true strain of 0.7 at strain rates of 0.1 and 1 s^{-1} using a hot deformation simulator (Thermec-master Z). The specimens were heated to the compression temperature at a rate of 5°C s^{-1} and held for 5 min to ensure temperature uniformity. The hot-compressed samples were quenched at room temperature using nitrogen gas.

After mechanical polishing of the cross-section of the CG and FG billets, the secondary phases were examined using scanning electron microscopy (SEM, ZEISS, Gemini 500) and energy dispersive X-ray spectroscopy (EDS) installed at the Center for University-wide Research Facilities (CURF) at Jeonbuk National University. The grain structure of the billet was analyzed using SEM (JEOL, JSM-7900F) equipped with an EBSD with a step size of 1 μm. To investigate the hot deformation behavior, the hot-compressed specimens were examined using EBSD with step sizes of 0.4 and 0.07 μm. The EBSD data were analyzed using TSL OIM analysis software, and the Al matrix and secondary phases (MgZn$_2$, Al$_{23}$CuFe$_4$, and Mg$_2$Si) were included in the analysis.

3. Results and discussion

Fig. 1(a) and (b) show the EBSD inverse pole figure (IPF) maps of the grain structure of the as-cast billets for the CG and FG alloys, respectively. The CG billet consists of coarse grains ~2 mm in size. The grains in the CG billet exhibit a feathery and columnar morphology in which two different grains are repeated, as reported for a DC casting 6063 Al alloy [18]. The misorientation angle between two adjacent columnar grains is 60°, indicating that the boundaries of adjacent columnar grains are twin boundaries [19]. The boundaries of the adjacent columnar grains are confirmed as Σ3 {111} twin boundaries, which indicates twinned dendrite growth during DC casting of the CG alloy. Meanwhile, the FG billet with Al–5Ti–1B grain refiners exhibits fine and equiaxed grains with a size of ~70 μm. The grains of the FG billet show a Mackenzie distribution, indicating a random grain-orientation distribution [20]. The grain refinement induced by adding the Al–5Ti–1B grain refiner can be explained by the enhancement of grain nucleation on the TiB$_2$ inoculant particles and grain restriction by excess Ti solutes [21,22].

Fig. 1(c) and (d) show SEM images of secondary phases formed during the solidification of CG and FG billets, respectively. The secondary phase of the CG and FG billets is mainly present at the twin and grain boundaries, where solute segregation occurs during solidification [23]. EDS analysis confirms that the secondary phase mainly comprises the η-Mg(Zn,Cu,Al)$_2$ phase with a few Mg$_2$Si and Al$_{23}$CuFe$_4$ phases. The total areal fraction of the secondary phase is almost identical at 9.5% for both alloys. However, the size of the secondary phase is smaller in the CG billet with numerous twin boundaries. The homogenization heat treatment causes the dissolution of secondary phases (mainly the η-Mg(Zn,Cu,Al)$_2$ phase), thereby reducing the areal fraction to 1.8% and 1.7% for the CG and FG alloys, respectively (Fig. 1(e) and (f)). The size of the secondary phase of the homogenized billet is smaller for the CG alloy (1-3 μm) than that for the FG alloy (2-6 μm).

Fig. 2(a) shows the change in the compressive strain–stress curves of the CG and FG alloys according to the hot compression temperature at a strain rate of 1 s^{-1}. Regardless of the alloy and
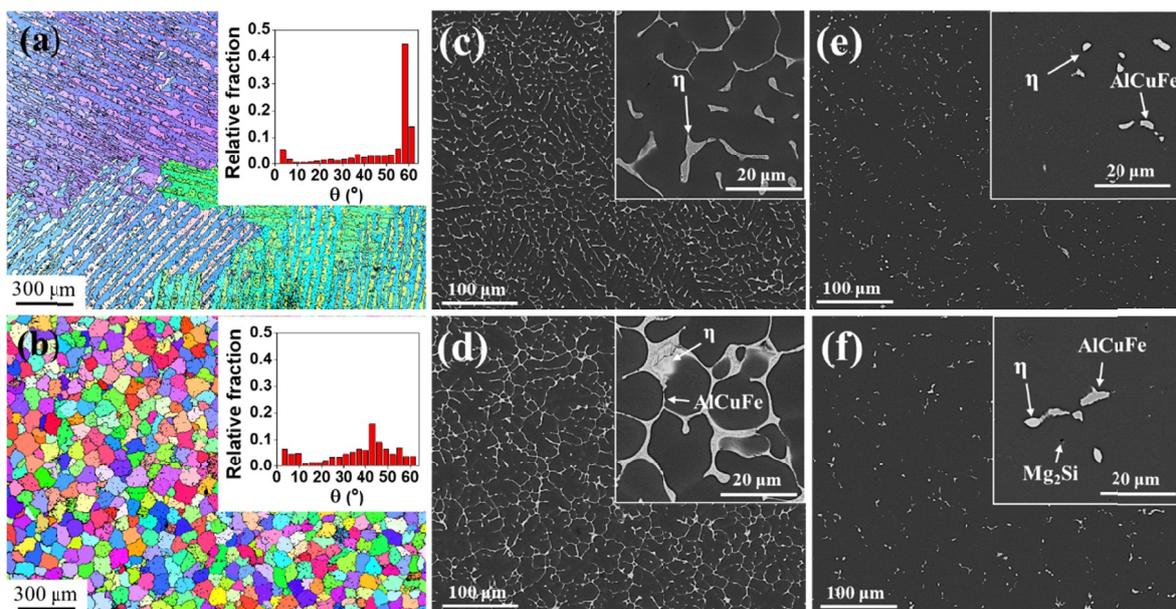

Fig. 1. Misorientation angle fraction histogram (inset) and EBSD IPF map of a cross-section of as-cast billet for (a) coarse-grained (CG) and (b) fine-grained (FG) alloys. SEM images of (c,d) as-cast and (e,f) homogenized samples for (c,e) CG and (d,f) FG alloys. Insets in (c-f) show the high-magnification image for the secondary phases
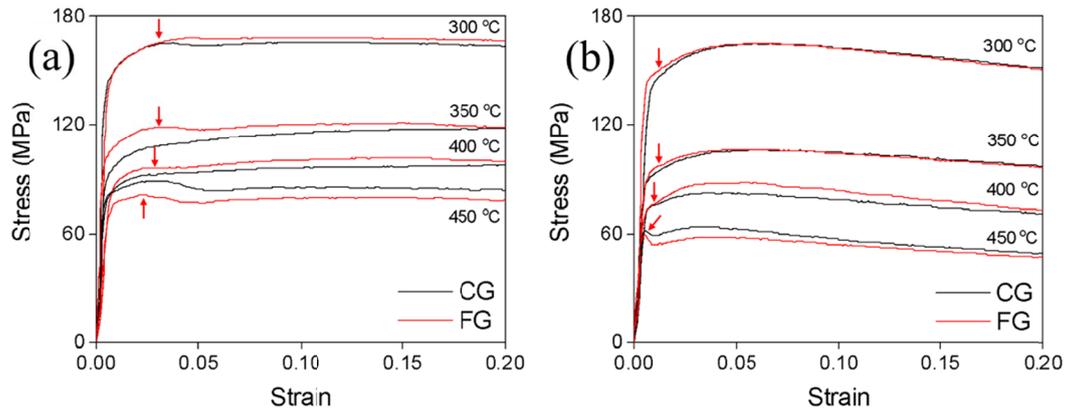
Fig. 2. Compressive stress-strain curves of coarse-grained (CG) and fine-grained (FG) alloys at 300-450°C, at strain rates of (a) 1 s^{-1} and (b) 0.1 s^{-1}. The red arrow indicates the peak stress at which dynamic recrystallization occurs

compression temperature, the stress increases because of work hardening [24,25] and then decreases because of softening by the onset of DRX, thereby forming a distinct peak [26]. The stress increases again with further compression because the work hardening rate is higher than the softening rate of DRX [27], followed by a dynamic flow-softening regime up to the end of straining [28]. The peak stress (marked by red arrows) decreases, and the strain at the peak stress decreases as the compression temperature increases from 300 to 450°C. The peak stress values at a strain rate of 0.1 s^{-1} (Fig. 2(b)) are lower at all compression temperatures than at a strain rate of 1 s^{-1}. The strain values at peak stress are also lower at lower strain rates. Compared to the CG alloy, the FG alloy exhibits higher peak stress and strain values at 300-400°C but lower at 450°C at both strain rates of 1 and 0.1 s^{-1}. This is related to the different hardening and softening behaviors during hot compression owing to the different solidification microstructures of the CG and FG billets [29].

Fig. 3 shows the IPF maps along the radial (RD) and compression (CD) directions for the hot-compressed CG and FG alloys. As shown in CD-IPF, the CG and FG alloys exhibit
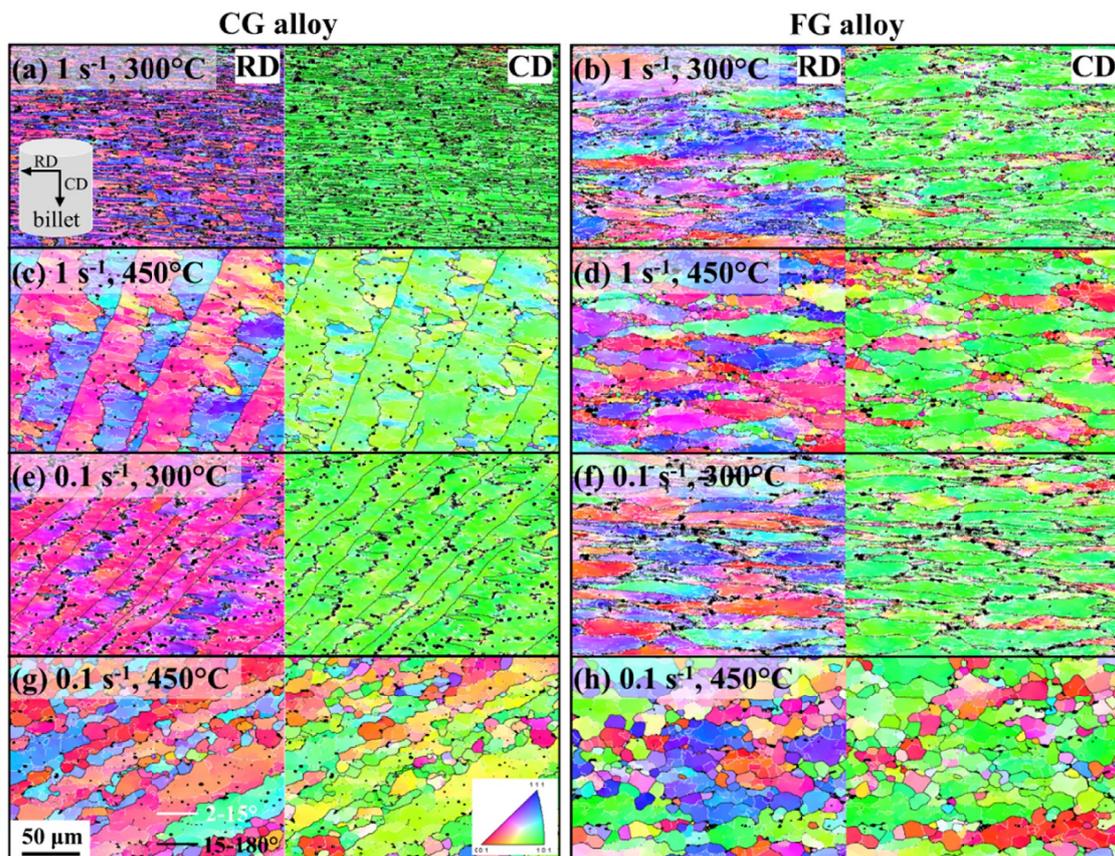

Fig. 3. IPF and grain boundary maps of (a,c,e,g) coarse-grained (CG) alloys and (b,d,f,h) fine-grained (FG) alloys deformed at (a,b) 300°C and (c,d) 450°C at a strain rate of 1 s^{-1} and deformed at (e,f) 300°C and (g,h) 450°C at a strain rate of 0.1 s^{-1}. Black phases indicate secondary phases, including MgZn$_2$, Al$_{23}$CuFe$_4$, and Mg$_2$Si

a strong <110> fiber texture, which corresponds to the typical compression texture of Al alloys [30,31]. FG alloys also contain a substantial number of <100> fiber textures, which are known to remain during compression at high temperatures and low strain rates [32]. Grains with a <100> fiber texture act as nucleation sites for DRX (Fig. 3(d)), which is in good agreement with a previous report [33]. Meanwhile, the grains with <100> fiber texture were not included in the EBSD analysis of the CG alloys because of their coarse-grain size (~2 mm). Fine Al grains with random orientations near the secondary phase (marked as black particles) or twin/grain boundaries correspond to the DRXed Al grains. DRX is enhanced at higher compression temperatures and lower strain rates [34,35].

Fig. 4(a) and (b) show high-magnification EBSD CD-IPF maps indicating the presence of DRXed grains near the secondary phases after deformation at 300°C for the CG and FG alloys, respectively. This suggests the occurrence of particle stimulated nucleation (PSN), which is active in secondary phases with a size of 4-12 μm [36]. The FG alloy exhibits a more DRXed region around the secondary phases than the CG alloys. The enhanced PSN in the FG alloy is attributed to coarser secondary phases (2-6 μm) suitable for PSN activation.

Fig. 4(c) shows the EBSD microstructure of the CG alloy deformed at 450°C. The cumulative misorientation toward the twin boundary (vector A) does not exceed 15°, indicating the occurrence of dynamic recovery (DRV). Continuous dynamic recrystallization (CDRX) is the process of conversion from low-angle grain boundaries (LAGB) to high-angle grain boundaries (HAGB) due to sub-grain rotation and growth during deformation [37,38]. CDRX has rarely been observed in CG alloys because of the difficulty of CDRX around twin boundaries [31]. However, in the FG alloy (Fig. 4(d)), the cumulative misorientation (vector B) gradually increases with distance and exceeds 15° at the HAGB. This indicates that CDRX actively occurs in FG alloys with numerous HAGB acting as sites for CDRX [39-41]. EBSD analysis confirms the enhanced DRX in the FG alloys due to the enhanced PSN and CDRX compared to the CG alloys. This DRX enhancement in the FG alloy is significant at 450 °C, where the driving force for DRX is high, resulting in reduced peak stress due to DRX-induced softening. The higher peak stress of the FG alloys at 300-400°C may be attributed to hardening by grain refinement prevailing over softening by the enhanced DRX.

4. Conclusions

We investigated the effect of adding Al–5Ti–1B grain refiners on the solidification microstructure and hot deformation behavior of a DC-cast Al–Zn–Mg–Cu alloy at 300-450°C. The addition of grain refiners significantly reduced the grain size from ~2 mm to ~70 μm and modified the grain morphology from coarse columnar twinned dendrites to fine equiaxed dendrites. Microstructural changes caused by the addition of grain refiners increased the size of the secondary phase from 1-3 μm to 2-6 μm, while the areal fraction remained unchanged. The peak stress due to the occurrence of DRX decreased with increasing compression temperature and decreasing strain rate for both the CG and FG alloys. The peak stress of the FG alloys is higher at 300-400°C and lower at 450°C than that of the CG alloys. EBSD analysis revealed that PSN and CDRX are enhanced in the FG alloys because of coarser secondary phases and many HAGBs, resulting in a lower peak stress at 450°C. Grain refinement hardening contributes to higher peak stresses of the FG alloys at compression temperatures of 300-400°C, where slight DRX occurs.
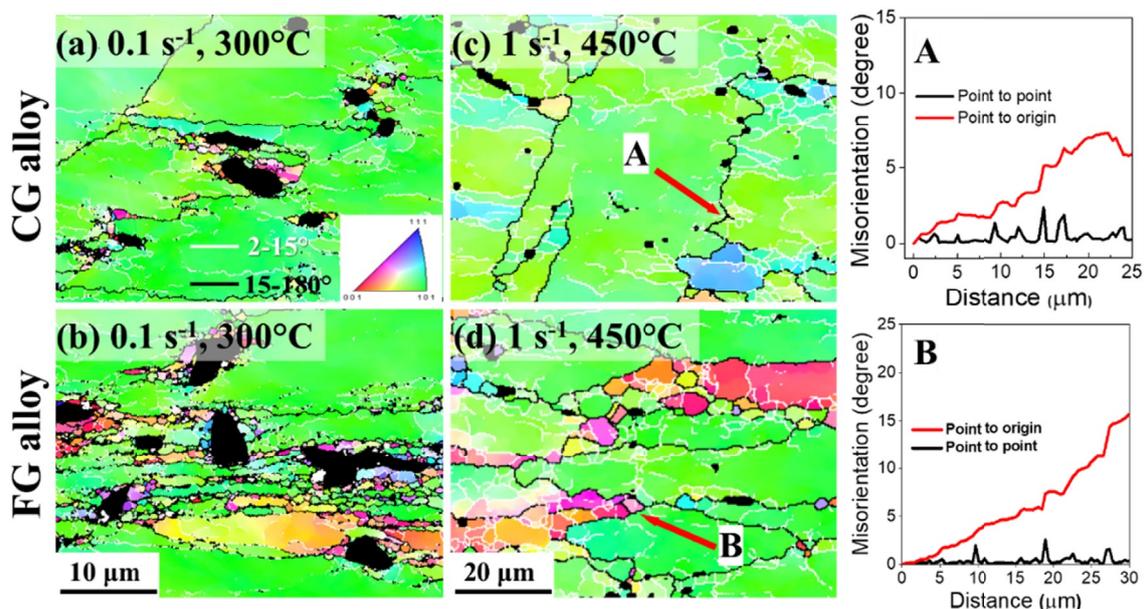

Fig. 4. EBSD IPF map showing particle-stimulated nucleation during deformation at 300°C (strain rate: 0.1 s^{-1}) of (a) coarse-grained (CG) and (b) fine-grained (FG) alloys. IPF map of (c) CG and (d) FG alloys deformed at 450°C (strain rate: 1 s^{-1}) and changes in misorientations along red arrows. Black phases indicate secondary phases, including MgZn$_2$, Al$_{23}$CuFe$_4$, and Mg$_2$Si

REFERENCES

[1] Y.L. Wu, F.H. Froes, A. Alvarez, C.G. Li, J. Liu, Mater. Des. **18**, 211-215 (1997).

[2] S.H. Lee, J.G. Jung, S.I. Baik, S.H. Park, M.S. Kim, Y.K. Lee, K. Euh, Mater. Sci. Eng. A **801**, 140437 (2021).

[3] X. Wang, Q. Pan, L. Liu, S. Xiong, W. Wang, J. Lai, Z. Huang, Mater. Charact. **144**, 131-140 (2018).

[4] X. Xu, J. Zheng, Z. Li, R. Luo, B. Chen, Mater. Sci. Eng. A. **691**, 60-70 (2017).

[5] B. Ke, L. Ye, J. Tang, Y. Zhang, S. Liu, H. Lin, X. Liu, J. Alloys Compd. **845**, 156113 (2020).

[6] W. Liu, H. Zhao, D. Li, Z. Zhang, G. Huang, Q. Liu, Mater. Sci. Eng. A. **596**, 176-182 (2014).

[7] Q. Contrepois, C. Maurice, J.H. Driver, Mater. Sci. Eng. A. **527**, 7305-7312 (2010).

[8] J. Zhao, Y. Deng, J. Tang, J. Zhang, J. Alloys Compd. **809**, 151788 (2019).

[9] G. Wang, X. Li, G. Yu, Z. Gu, Mater. Lett. **321**, 132413 (2022).

[10] B. Ke, L. Ye, J. Tang, Y. Zhang, S. Liu, H. Lin, X. Liu, J. Alloys Compd. **845**, 156113 (2020).

[11] C.Y. Kang, T.J. Yoon, M.C. Kang, J. Powder Mater. **20** (4), 302-307 (2013).

[12] R. Nadella, D.G. Eskin, Q. Du, L. Katgerman, Prog. Mater. Sci. **53**, 421-480 (2008).

[13] L. Yang, S. Li, Y. Li, K. Fan, H. Zhong, J. Mater. Res. **34**, 240-250 (2019).

[14] S. Henry, T. Minghetti, M. Rappaz, Acta Mater. **46**, 6431-6443 (1998).

[15] M. Kumar, N.G. Ross, J. Mater. Process. Technol. **231**, 189-198 (2016).

[16] O.N. Senkov, R.B. Bhat, S.V. Senkova, J.D. Schloz, Metall. Mater. Trans. A **36**, 2115-2126 (2005).

[17] M.S. Kim, S.H. Lee, J.G. Jung, K. Euh, Prog. Nat. Sci. **31**, 434-441 (2021).

[18] S. Kumar, K.A.Q O'Reilly, Mater. Charact. **120**, 311-322 (2016).

[19] L. Li, Y. Zhang, C. Esling, Z. Zhao, Y. Zuo, H. Zhang, J. Mater. Sci. **44**, 1063-1068 (2009).

[20] J. Mason, C. Schuh, Acta Mater. **57**, 4186-4197 (2009).

[21] S.B. Kim, J. G. Jung, Y.H. Cho, S.H. Kim, K. Euh, J.M. Lee, Met. Mater. Int. **28**, 1549-1560 (2022).

[22] J. Li, F.S. Hage, Q.M. Ramasse, P. Schumacher, Acta Mater. **206**, 116652 (2021).

[23] A. Lervik, S. Wenner, O. Lunder, C.D. Marioara, R. Holmestad, Mater. Charact. **170**, 110695 (2020).

[24] S.S. Hansen, Fundamentals of Microalloying Forging Steels, G. Krauss and S.K. Banerji, eds., TMS-AIME, New York, NY, pp. 155, 1987.

[25] N. Seo, J. Lee, W. Shin, J. Jeon, J. Park, S.B. Son, J.G. Jung, S.J. Lee, J. Powder Mater. **29** (5), 382-389 (2022).

[26] L. Wang, F. Liu, Q. Zuo, C. F. Chen, Mater. Des. **47**, 737-745 (2013).

[27] H. Mirzadeh, A. Najafizadeh, M. Moazeny, Metall. Mater. Trans. A **40**, 2950-2958 (2009).

[28] M.R. Rokni, A. Zarei-Hanzaki, A.A. Roostaei, A. Abolhasani, Mater. Des. **32**, 4955-4960 (2011).

[29] D. Feng, X.M. Zhang, S.D. Liu, Y.L. Deng, Mater. Sci. Eng. A. **608**, 63-72 (2014).

[30] E.A. Calnan, Acta Metall. **2**, 865-874 (1954)

[31] J.X. Zhang, K.L. Zhang, Y.T. Liu, L. Zhong, Rare Met. **33**, 404-413 (2014)

[32] Y. Huang, F.J. Humphreys, M. Ferry, Acta Mater. **48**, 2543-2556 (2000).

[33] I. Samajdar, R.D. Doherty, Acta Mater. **46**, 3145-3158 (1998).

[34] G.Z. Quan, Y. Wang, Y.Y. Liu, J. Zhou, Mater. Res. **16**, 1092-1105 (2013).

[35] Q. Zang, H. Yu, Y.S. Lee, M.S. Kim, H.W. Kim, Mater. Charact. **151**, 404-413 (2019).

[36] X. Lei, Y. Zhang, J. Sun, F. Bachmann, X. Yang, R.E. Sanders, D. Juul Jensen, Mater. Res. Lett. **9**, 65-70 (2021).

[37] S. Liu, Q. Pan, M. Li, X. Wang, X. He, X. Li, J. Lai. Mater. Des. **184**, 108181 (2019).

[38] D.H. Yang, G.S. Ham, S.H. Park, K.A. Lee. J. Powder Mater. **28** (4), 301-309 (2021).

[39] K.E. Huang, R.E. Logé, Mater. Des. **111**, 548-574 (2016).

[40] F.J. Humphreys, M. Hatherly. Recrystallization and related annealing phenomena, 2nd edn. Elsevier, Oxford, 2012.

[41] S. Gourdet, F. Montheillet, Mater. Sci. Eng. A. **283**, 274-288 (2000).